

Evaluation of the Oxygen Migration Energy in Doped Ceria by Terahertz Spectroscopy

Masaya Nagai^{1,2,*}, Yuto Furutani,¹ Hikaru Takehara,¹ Tomohide Morimoto,¹ Masaaki Ashida,¹ Yuji Okuyama³, and Yukimune Kani⁴

¹ Graduate School of Engineering Science, Osaka University, Toyonaka, Osaka 560-8531, Japan

² Panasonic Science Research Alliance Laboratories, Graduate School of Engineering, Osaka University, Suita, Osaka 565-0871, Japan

³ Research Center for Sustainable Energy & Environmental Engineering, Faculty of Engineering, University of Miyazaki, 1-1 Gakuenkibanadai-nishi, Miyazaki 889-2192, Japan

⁴ Technology Division, Panasonic Corporation, 3-1-1 Yagumo-nakamachi, Moriguchi City, Osaka 570-8501, Japan



(Received 10 August 2021; revised 7 December 2021; accepted 8 December 2021; published 30 December 2021)

We measure the terahertz conductivity of doped ceria by terahertz time-domain spectroscopy at different temperatures to characterize the shape of the potential associated with microscopic ion hopping. The experimental results for Gd- and La-doped ceria show that the activation energy in doped ceria is larger than that in stabilized zirconia. This result can be explained by a simple rigid-body model with the assumption of doping-induced lattice expansion, i.e., by considering the gap between cations. Our results for conventional fluorite-type solid-oxide electrolytes show that terahertz spectroscopy can be used to investigate fast microscopic ionic conduction in various electrolytes, which cannot be accessed through conventional impedance measurements.

DOI: 10.1103/PhysRevApplied.16.064069

I. INTRODUCTION

Fast ionic conduction in solids has attracted attention in the field of fuel cells and all-solid-state batteries [1–3] because ionic conductors can exhibit higher ionic conductivities than aqueous solutions and are usually chemically, mechanically, and thermally stable. A comprehensive understanding of the ionic conduction mechanism in crystalline solids is required for the design of solid electrolytes [4]. In general, ionic conduction in solids is described by the hopping of an ion between atomic sites, and the activation energy required to overcome the potential barriers can be used to characterize ionic transport. Such potential barriers are experimentally evaluated using ac impedance measurements and diffusion measurements, but these measurements mainly provide information about long-distance ionic conduction that is a result of several short-distance ion jumps. On the other hand, ion transport in crystalline solids is theoretically described as a process with a wide dynamic range from microscopic vibrations of atoms to ion jumps between atomic sites [3,5].

Recently, we demonstrated that terahertz (THz) spectroscopy was a powerful method that allowed us to directly characterize fast ionic motion on the picosecond timescale

[6]. We measure the THz conductivity of stabilized zirconia, which is the most widely used electrolyte in commercial solid-oxide fuel cells [2,7,8]. The THz conductivity of stabilized zirconia is related to the individual hopping of an oxygen ion to an unoccupied site, and the activation energy evaluated from THz conductivity is interpreted as the average minimum-potential barrier for hopping to an unoccupied site, and this value is close to the so-called migration energy. We find that the activation energy for individual hopping decreases with an increase of the ionic radius of the dopant. The reason for this trend is that dopants with large ionic radii expand the gap between host cations in stabilized zirconia, resulting in a decrease in migration energy. THz spectroscopy on other materials is required to verify if this model and characterization method are also applicable to other solid-oxide electrolytes.

Ceria (CeO_2) is a solid-oxide electrolyte that has been considered for use in fuel cells because its ionic conductivity is higher than that in stabilized zirconia [2,5,9,10]. As shown in Fig. 1, ceria has the same fluorite crystal structure as that of stabilized zirconia. As a host cation, cerium (Ce) has a larger ionic radius ($r_c = 0.97 \text{ \AA}$) than that of zirconium ($r_c = 0.84 \text{ \AA}$) [11]. Therefore, the gap between cations in ceria should be smaller [12], which should have an influence on the microscopic migration of ions. Here, we perform THz conductivity measurements on nondoped

* mnagai@mp.es.osaka-u.ac.jp

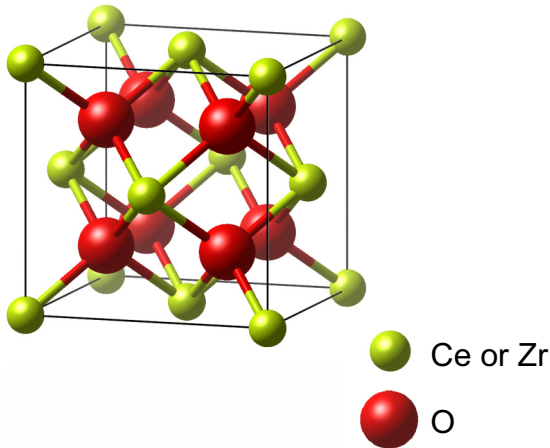


FIG. 1. Schematic of the crystal structure of cubic ceria and zirconia in the stick-and-ball scheme.

and doped ceria sintered pellets to directly verify the influence of the gap between cations on the THz activation energy compared to doped zirconia.

II. SAMPLE PREPARATION AND INITIAL CHARACTERIZATION

In our experiments, we measure the THz conductivity of nondoped CeO_2 , $\text{Ce}_{0.84}\text{Gd}_{0.16}\text{O}_{2-\delta}$ (GDC), and $\text{Ce}_{0.84}\text{La}_{0.16}\text{O}_{2-\delta}$ (LDC) sintered pellets, in which the dopant concentrations are the same as that of the M -stabilized zirconia $\text{Zr}_{0.84}\text{M}_{0.16}\text{O}_{2-\delta}$ in Ref. [6]. First, GDC and LDC powders are prepared by liquid-state reactions and calcination at 900 °C for 10 h in air. Then, the pellets are sintered in air at 1300 °C for 10 h. For the nondoped CeO_2 pellet, commercial powder (Kojundo Chemical Laboratory Co., Ltd.) is compacted by cold isostatic pressing at 200 MPa and sintered in air at 1300 °C for 10 h. The diameters of the pellets are larger than the diameter of the aperture (10 mm) of the metallic sample holders, and their thicknesses are 0.875 mm for nondoped CeO_2 , 0.690 mm for GDC, and 0.699 mm for LDC. We also measure the THz conductivity of a Gd-stabilized zirconia, $\text{Zr}_{0.84}\text{Gd}_{0.16}\text{O}_{2-\delta}$ (GSZ), sintered pellet for comparison.

For the initial characterization of our sintered pellets, we measure the x-ray diffraction (XRD) patterns of the powder samples with $\text{CuK}\alpha$ radiation (MinFlex600, Rigaku). The XRD patterns are analyzed by employing the Rietveld refinement technique. The results are shown in Fig. 2(a). The observed XRD signals of the samples are characteristic of the cubic fluorite structure. We add the inorganic crystal structure database (ICSD) XRD data of CeO_2 (ICSD180955) and ZrO_2 (ICSD173962) as vertical bars. The lattice constants evaluated by Rietveld refinement are 5.41 Å for nondoped ceria, 5.423 Å for GDC, and 5.468 Å for LDC. These values are larger than the value

of 5.156 Å for GSZ. We also characterize them from their SEM photographs, as shown in Fig. S1 within the Supplemental Material [13], indicating that the grain size is larger than several hundreds of nanometers. Since no grain-size dependence of the conductivity is reported above 70 nm [14], our samples exhibit ionic conductivity as a typical solid electrolyte.

Furthermore, we characterize the phonon frequencies of ceria and zirconia by conventional infrared spectroscopy. Figure 2(b) shows the infrared reflection spectra of nondoped CeO_2 , GDC, and LDC sintered pellets at room temperature. These spectra are measured by using two Fourier-transform infrared (IR) spectrometers [JASCO FT/IR-4100 (400–8000 cm⁻¹), and JASCO SMMPFTS-4 (100–400 cm⁻¹)]. It is reported that cubic ceria has one IR-active phonon mode at 283 cm⁻¹ (T_{2u}) and multiphonon absorption components in the frequency range of 300–400 cm⁻¹ [15–17], which cause the characteristic Reststrahlen band, extending from 8 to 18 THz in Fig. 2(b). We characterize these modes from the infrared reflection spectrum of our nondoped CeO_2 , as shown in Fig. S2 within the Supplemental Material [13], and confirm these mode assignments. The spectra of doped ceria [Fig. 2(b), black and blue curves] show that the spectral position of the high-reflection band, corresponding to the Reststrahlen band, is the same as that of nondoped ceria [Fig. 2(b), red curve]. However, their reflectivity is lower. A similar spectral modulation is reported for 1-mol% Ca-doped ceria [16], and it is due to the large phonon damping caused by dopants and oxygen vacancies. It is also caused by the localized mode related to the attempted ion hopping [18], although the theoretical attempt frequency is slightly lower [19,20]. The sub-THz frequencies at which we measure the conductivities in this work are smaller than the frequencies of the phonons and the attempt resonance. We also add the reflection spectrum of GSZ. It shows a Reststrahlen band at frequencies between 8 and 23 THz [6]; this is located at slightly higher frequencies than that obtained for ceria.

We measure the THz conductivities of the sintered pellets by THz time-domain spectroscopy with ultrashort optical pulses [21]. Figure 3(a) shows the experimental setup. Here, we use the second-harmonic output of an Er-doped fiber laser system (TOPTICA Photonics, FemtoFiber pro NIR). The pulses have a center wavelength of 780 nm, a repetition rate of 80 MHz, an average power of 130 mW, and a pulse duration of 90 fs. The output beam is split into two beams for THz generation and detection by electro-optic (EO) sampling. The beam for THz generation is focused on an InAs crystal under a magnetic field of 0.4 T to generate THz pulses via the photo-Dember effect. The generated THz pulses are collimated by an off-axis parabolic mirror with a focal length of 50 mm and focused on the sample by an off-axis parabolic mirror with a focal length of 300 mm (the mirrors are not shown in the figure).

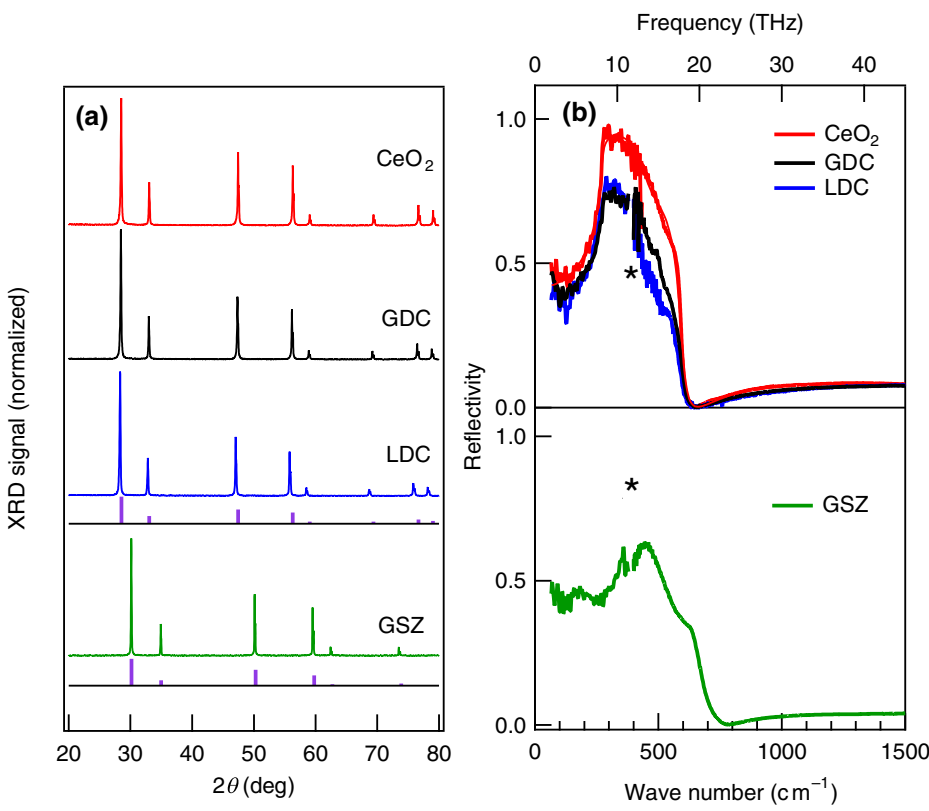


FIG. 2. (a) XRD patterns of non-doped CeO₂, GDC, LDC, and GSZ sintered pellets. All patterns are characteristic of the cubic fluorite structure. Data are offset for clarity. XRD data of CeO₂ (ICSD180955) and ZrO₂ (ICSD173962) are added with vertical violet bars. (b) Infrared reflection spectra of the four samples. Large noise around 400 cm⁻¹ (denoted by the asterisk) is due to low sensitivity of the two infrared interferometers.

The sample is mounted in a silica tube inserted into an electric furnace (NETSUDEN KOURYOU Co., Ltd.) and the temperature of dry air flowing in the tube (2 l/min, pressure $p_{O_2} = 0.2$ atm) was controlled up to 1073 K with a heating rate of 4 K/min. This electric furnace is different from that in Ref. [6]. The transmitted THz pulses are focused on a 2-mm-thick (110)-oriented ZnTe crystal, the THz-induced birefringence of which is detected by using a quarter-wave plate, a Wollaston prism, and two photodetectors. The resident excitation laser from the emitter and the black-body radiation from the sample are blocked by two thin black polypropylene films (not shown in the figure). The time delay of the THz pulse is controlled by a delay stage in the optical path of the beam for THz generation. To improve the signal-to-noise ratio, the THz light is modulated at 2703 Hz using an optical chopper.

The black curve in Fig. 3(b) shows the electric field waveform of the THz pulse transmitted through the silica tube without sample, $E_r(t)$, which serves as the reference. We confirm that the power spectrum of $E_r(t)$ is almost independent of the temperature of the electric furnace, but the temporal position of the zero crossing of $E_r(t)$ near its maximum at 1073 K is delayed by 0.4 ps with respect to that at room temperature due to the refractive-index change of the gas and the silica tube in the optical path (Figs. S3 and S4 within the Supplemental Material [13]). Based on data in Fig. S4 within the Supplemental Material [13], we adjust the temporal position of the recorded time-domain electric field profiles in such a way to remove the delay

induced by this refractive-index change. The waveform of the THz pulse that is transmitted through the sample in the electric furnace and includes the adjustment of the temporal position is denoted by $E_s(t)$. The blue curve in Fig. 3(b) is $E_s(t)$ for the GDC sample at 310 K, and the red curve is that at 1073 K. We can confirm that, at both temperatures, the amplitude of $E_s(t)$ is smaller and delayed with respect to $E_r(t)$. This change in $E_s(t)$ appears because the THz pulse passes through the pellet with a complex dielectric constant, $\tilde{\epsilon}(\omega)$. Therefore, $\tilde{\epsilon}(\omega)$ can be directly evaluated from complex transmittance $\tilde{t}(\omega)$, which is the ratio of the Fourier transform of $E_s(t)$, $\tilde{E}_s(\omega)$, to that of $E_r(t)$, $\tilde{E}_r(\omega)$ [22,23]:

$$\tilde{t}(\omega) = \frac{\tilde{E}_s(\omega)}{\tilde{E}_r(\omega)} = \frac{4\sqrt{\tilde{\epsilon}(\omega)}}{\left[\sqrt{\tilde{\epsilon}(\omega)} + 1\right]^2} \exp \left\{ \frac{i \left[\sqrt{\tilde{\epsilon}(\omega)} - 1 \right] d\omega}{c} \right\}. \quad (1)$$

Here, c is the speed of light in a vacuum and d is the sample thickness. In our analysis, we perform the Fourier transform of an electric field in a limited time range to neglect the internal reflections in the sample. Thus, together with knowledge of the background dielectric constant, ϵ_∞ , we can evaluate the complex conductivity, $\tilde{\sigma}(\omega) = i\omega[\tilde{\epsilon}(\omega) - \epsilon_\infty]$, directly. The real part of the conductivity is denoted by σ .

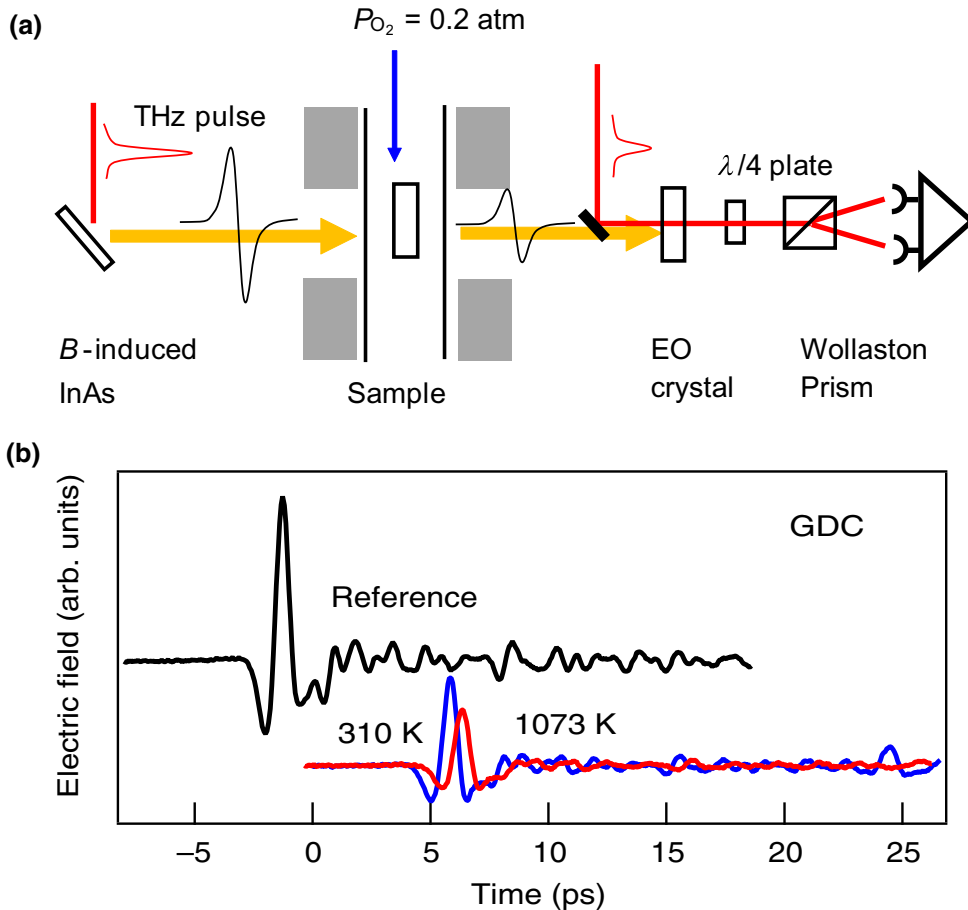


FIG. 3. (a) Experimental setup for THz time-domain spectroscopy. (b) Time-domain profiles of the THz pulses obtained without (black curve) and with the GDC sintered pellet inside the electric furnace (red and blue curves). Time-domain profiles in this plot can be compared because we remove the time delay caused by the change in the optical path length due to the heated gas and silica tube inside the electric furnace.

III. RESULTS

Figures 4(a) and 4(b) show the real part of the conductivity in GDC and LDC, respectively, as a function of frequency for different temperatures. Overall, the THz conductivity increases with frequency, which is mainly due to the transverse-optical (TO) resonance at 8 THz. In the case of a Lorentz model for the phonon resonance, the conductivity should be proportional to the square of the frequency, ν , in the lower-frequency region. However, the slopes observed in the low-frequency region in Figs. 4(a) and 4(b) are smaller at higher temperatures; the THz conductivities increase with temperature, especially in the low-frequency region, and this causes a reduction of the slope. This behavior is similar to that of stabilized zirconia [6] and cannot be explained by a temperature-dependent spectral broadening of the TO phonon mode at 8 THz.

As explained below, we consider that electronic conduction at higher temperatures is not the cause of this deviation from a quadratic dependence. It is known that ceria exhibits reduction and oxidation at high temperatures [24], and that this causes electronic conduction [25]. However, we can neglect electronic conduction in ceria under the experimental conditions of an oxygen partial pressure of 0.2 atm and temperatures below 1073 K. This can be

confirmed in Fig. 4(c), which shows the THz conductivity spectra of nondoped CeO_2 at different temperatures. We add the theoretical curve extrapolated from the analysis of the infrared reflection in Fig. S2 within the Supplemental Material [13] as a dashed line. The THz conductivity is larger than the extrapolation curve, suggesting the existence of different conductivity components, such as defects [26]. Here, we emphasize that the observed temperature dependence is weak. This suggests that the THz conductivity of nondoped CeO_2 is not dominated by electronic contributions. Therefore, we conclude that the observed THz conductivities of GDC and LDC at high temperatures originate from ionic motion and not from electronic motion.

Figure 5(a) shows the temperature dependences of the THz conductivities of our four samples at 0.34 THz. Notably, the horizontal axis of this plot is the inverse of the sample temperature, $1/T$. GSZ, GDC, and LDC exhibit a relatively large temperature dependence compared with nondoped ceria. We evaluate the activation energy, E_a , by conventional Arrhenius analysis. We define $\sigma = (A/T)\exp[-E_a/k_B T] + C$, where C is the nonconductive component (due to phonons etc.) Due to phonon resonances, the THz conductivity data of GDC and LDC

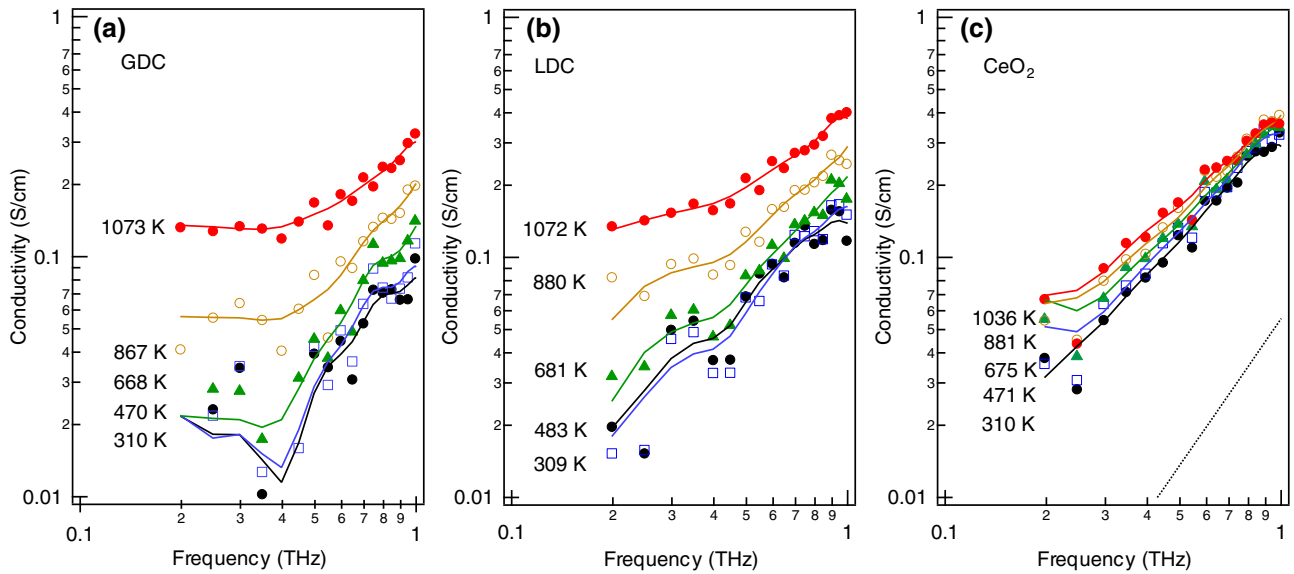


FIG. 4. THz conductivity spectra of (a) GDC, (b) LDC, and (c) nondoped ceria sintered pellets at different temperatures. Solid smoothing curves are guides to the eye. Dashed line in (c) is the fitted curve analyzed with the two Lorentz oscillators from the mid-infrared reflection, as shown in Fig. S2 within the Supplemental Material [13].

do not lie on a straight line in the low-temperature region ($T < 800$ K). On the other hand, they lie on a straight line at high temperatures. Therefore, we fix C to the conductivity at room temperature and evaluate the activation energy from conductivity data in the temperature range above 830 K. The obtained activation energies are 0.54 eV for GDC and 0.44 eV for LDC. The result for the GSZ sintered pellet is about 0.31 eV. The conductivity spectra of this sample are shown in Fig. S5 within the Supplemental Material [13] and reproduce our previous result reported in Ref. [6]. Figure 5(b) shows the THz activation energies of the doped ceria samples and stabilized zirconia as a function of the dopant-ion radius. The values of THz activation energies of doped ceria are larger than those of doped zirconia upon decreasing the ionic radius of the dopant.

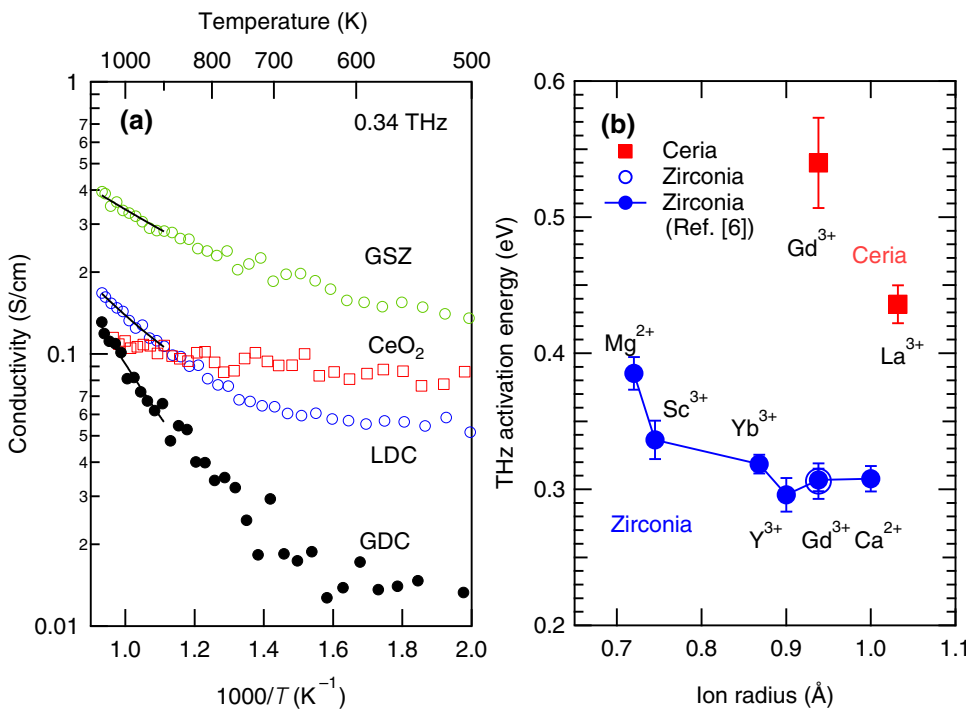
IV. DISCUSSION

Oxygen ions near a vacancy oscillate thermally at the so-called attempt frequency, ν_0 , before hopping occurs. Since the vacancy modes have strong anharmonicity, a vacancy oscillation with a large amplitude at high temperatures induces hopping to adjacent sites. This motion is also characterized in ceria by kinetic Monte Carlo simulations [19,20]. Thus, we consider that, also in ceria, the activation energy estimated from the THz conductivity corresponds to the average minimum-potential barrier for an unoccupied site. Below we discuss the validity of this assignment.

There are several reports on the migration energy in Y-doped ceria. Wang *et al.* reported a migration energy of 0.61 eV [27], and Adler and Smith reported 0.49 eV

[28]. Fuda *et al.* also determined a migration energy of 0.5 eV by nuclear magnetic resonance [29]. Nakayama and Martin calculated the potential barrier using the nudged-elastic-band method and pointed out that a straightforward migration path between two adjacent oxygen sites exhibited the lowest activation energy; this energy is 0.5 eV [30]. The activation energies obtained from our THz conductivity spectra are almost the same as these previously reported values.

We also briefly consider the physical origin of the difference between our results and the results of the ac impedance measurements at high temperature for zirconia; for example, the THz activation energy for zirconia in Ref. [6] (approximately 0.3 eV) is smaller than the well-known migration energy of 0.6 eV [31]. Notably, the results of systematic ac impedance measurements in zirconia [32] show that there are fundamental issues that cannot be explained by the commonly used model of dopant-vacancy interactions [4]. One plausible explanation for the observed difference between the activation energies determined by THz spectroscopy and ac impedance measurements is that an ion can move faster in the vicinity of a dopant. Pornprasertsuk *et al.* calculated the saddle-point energy for Y-stabilized zirconia in various atomic arrangements [33]. The saddle-point energy of oxygen migration between two Zr atoms is 0.6 eV [see illustration in Fig. 6(a)], and that of oxygen migration along the edge of a dopant with large ionic radius is larger due to the narrower gap between cations. Furthermore, the saddle-point energy is lower when a Y dopant is located at a nearest-neighbor site of the start or destination oxygen site. Similar behavior is obtained in simulations for



ceria [20]. This implies faster oxygen-ion hopping between specific sites near a dopant. Such a local potential shape for ion hopping may not be detectable by high-temperature ac impedance measurements when assuming the ions are not influenced by the dopant. On the other hand, THz conductivity measurements are sensitive to it.

Since it is difficult to characterize the gap distance between specific cation sites experimentally, we discuss the activation energy in terms of the average distance based on the material's lattice constant. As shown in Fig. 6(a), the oxygen ion at the center of the cation tetrahedron hops to the adjacent unoccupied site via the saddle point of the potential. Since numerical simulations suggest that the energy at the saddle point between two host cations constitutes the lowest potential barrier [20,33], it should be possible to express the energy required for migration to the adjacent site as a function of the gap distance, g , between two host cations with radius r_c . If we assume that high-density doping causes a change in the lattice constant without any local strain, the gap distance, g , can be written as

$$g = \frac{\sqrt{2}a}{2} - 2r_c, \quad (2)$$

where we used the rigid-sphere model [12]. According to Eq. (2), g decreases with the cation radius, r_c , and thus g for ceria is smaller than that for zirconia. The gap distances are $g \approx 1.95 \text{ \AA}$ for zirconia and $g \approx 1.90 \text{ \AA}$ for ceria using an oxygen-ion radius of $r_O = 1.38 \text{ \AA}$. We plot the activation energies of doped ceria as a function of g in Fig. 6(b). For

FIG. 5. (a) Optical conductivity at 0.34 THz as a function of temperature for GDC, LDC, non-doped ceria, and GSZ sintered pellets. Accuracy of the measured conductivity is 0.02 S/cm. Black lines are those fitted through the least-squares method. (b) THz activation energy as a function of dopant radius for doped ceria and stabilized zirconia.

comparison, the activation energies of cubic zirconia with trivalent dopants are also plotted. This figure suggests that the THz activation energy decreases as g increases.

Our results are consistent with the expected influence of the dopant on the migration energy. We investigate the dopant dependence of the THz activation energy in stabilized zirconia and show that the migration energy decreases for larger dopant-ion radii [6], and similar behavior is confirmed for ceria, as shown in Fig. 5(b). It is reasonable from the viewpoint of the gap distance between cations. In general, the lattice constant of the host crystal increases for a dopant with a larger ionic radius. This is also supported by the lattice constants of doped ceria evaluated from the XRD patterns in Fig. 2(a). Yoshida *et al.* showed that there was a clear relationship between the ionic radius of the dopant and the lattice constant in Ce_{0.8}M_{0.2}O_{2-δ} [34]. Since the ionic radius of La is larger than that of Gd, the gap distance, g , between the cations in LDC is larger than that in GDC, according to Eq. (2), and this causes the smaller THz activation energy in LDC. Such knowledge of the effect of gaps on conductivity shows the direct relationship between local lattice structure and ion hopping.

The dopant-concentration dependence of THz conductivity can be used to verify this interpretation of the results. For this, we first measure the XRD patterns and the temperature dependences of the conductivity of stabilized zirconia with different Y₂O₃ concentrations at 0.36 THz (Fig. S6 within the Supplemental Material [13]). The activation energies are in the range 0.30–0.32 eV. There is no clear dependence of the activation energy on the

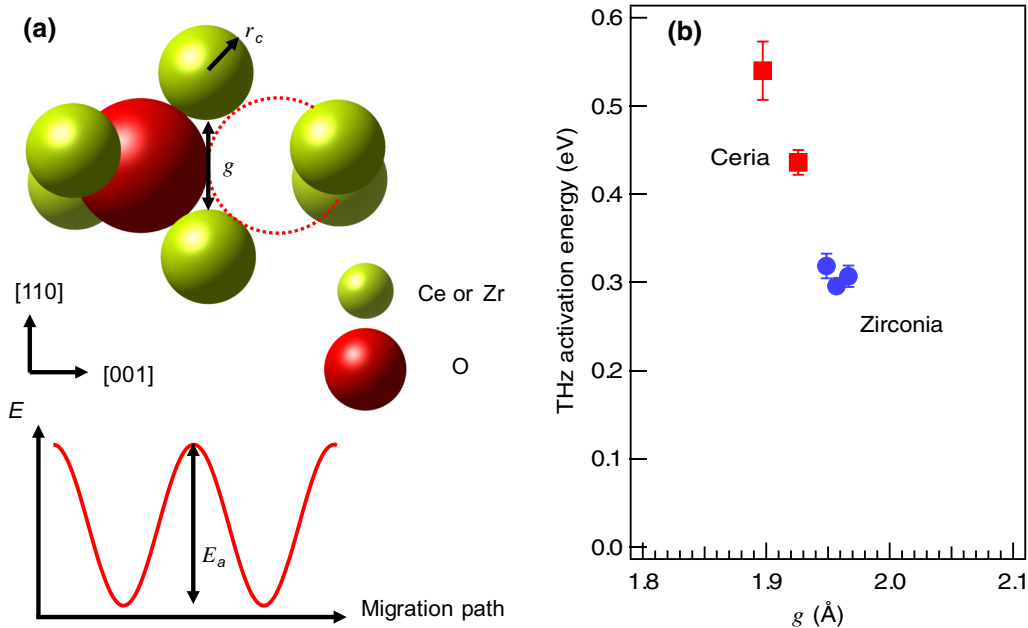


FIG. 6. (a) Illustration at the top shows the local structure around the mobile oxygen ion in the fill-space scheme. Graph at the bottom shows the potential on the migration path along the [001] direction. (b) THz activation energy as a function of g .

Y_2O_3 concentration because g (derived from the lattice constant evaluated by XRD) does not change upon doping with Y_2O_3 . The behavior of $\text{Ce}_{1-x}\text{Gd}_x\text{O}_{2-\delta}$ should be the same. Therefore, we additionally perform measurements for $\text{Ce}_{0.8}\text{La}_{0.2}\text{O}_{2-\delta}$, in which g is expected to change significantly with dopant concentration (Fig. S7 within the Supplemental Material [13]). The gap distance derived from the lattice constant of 5.480 Å is $g = 1.935 \text{ \AA}$, and the THz activation energy is 0.41 eV. The result of a lower THz activation energy for a larger gap supports the validity of our model.

Next, we discuss the difference between the shapes of the potential that governs the hopping process in ceria and zirconia. If we describe the individual potential at each site by a Morse potential for simplicity, the potential barrier can be considered proportional to v_0/χ , where χ is the characteristic anharmonic coefficient [35]. The attempt frequency, v_0 , in zirconia is about 11 THz, according to experiments [36]. In ceria, an attempt frequency of a few THz is theoretically predicted [20]. As mentioned in the explanation of Fig. 2(b), the attempt frequency is just above the TO phonon resonance because localized modes are located in the stop band of the crystal mode [18]. Numerical simulations suggest that the cations oscillate at a frequency of 10 THz in zirconia [37] and at 7 THz in ceria [15,16]. These values are mainly determined by the cation masses of 91 u for Zr and 140 u for Ce. As shown in Fig. 2(b), we experimentally characterize the TO phonon modes by infrared reflection spectroscopy and confirm them at 8 THz for ceria and 10 THz for zirconia.

Therefore, the attempt frequency for ceria appears at a lower frequency than that for zirconia. Furthermore, the estimated THz activation energy in GDC is larger than that in GSZ. Based on the THz activation energy, the attempt frequency, and the above assumption of the Morse potential, we find that the anharmonic coefficient, χ , for GDC is smaller than that for GSZ. The smaller χ for doped ceria is mainly due to the narrower gap between the cations of the host crystal in ceria.

Finally, we discuss the significance of THz conductivity in the material design of fuel cells and all-solid-state batteries from our results. We conclude that the evaluated activation energy in ceria is higher than that in zirconia, while the migration energy in ceria evaluated with conventional ac impedance measurements is smaller. This is clear evidence that the activation energy depends on the timescale of ion motion for the measurements [3]; the results from ac impedance measurements represent the average of the potential shapes of the sites in long-distance ionic transport, and the results of THz spectroscopy represent the direct motion of ions on a picosecond timescale. We confirm that THz spectroscopy directly reveals fast ionic conduction, which is directly related to the performance of fuel cells and all-solid-state batteries.

V. CONCLUSIONS

We measure the conductivity spectra of GDC, LDC, and nondoped CeO_2 by THz time-domain spectroscopy and characterize the THz activation energy, which is

equivalent to the migration energy. We find that the activation energy in doped ceria is larger than that in doped zirconia. It is different from the migration energy obtained through conventional ac impedance measurements. However, we explain that our experimental results can be interpreted in terms of the gap distance between cations. In addition, we show that the anharmonic coefficient for GDC is smaller than that for GSZ. We demonstrate that THz spectroscopy can be used to characterize typical solid-oxide electrolytes, and the evaluated information cannot be accessed through conventional ac impedance measurements. This technique is applicable to the development of lithium-ion conductors [3] because it can be used to characterize ultrafast ionic motion, which is decisive for the performance of all-solid-state batteries.

ACKNOWLEDGMENTS

This work is supported by JSPS KAKENHI Grant No. JP21H01015.

- [1] B. C. H. Steele and A. Heinzel, Materials for fuel-cell technologies, *Nature* **414**, 345 (2001).
- [2] A. Weber and E. Ivers-Tiffee, Materials and concepts for solid oxide fuel cells (SOFCs) in stationary and mobile applications, *J. Power Sources* **127**, 273 (2004).
- [3] Y. Gao, A. M. Nolan, P. Du, Y. Wu, C. Yang, Q. Chen, Y. Mo, and S.-H. Bo, Classical and emerging characterization techniques for investigation of Ion transport mechanisms in crystalline fast ionic conductors, *Chem. Rev.* **120**, 5954 (2020).
- [4] V. V. Kharton, F. M. B. Marques, and A. Atkinson, Transport properties of solid oxide electrolyte ceramics: A brief review, *Solid State Ionics* **174**, 135 (2004).
- [5] L. Malavasi, C. A. J. Fisher, and M. S. Islam, Oxide-ion and proton conducting electrolyte materials for clean energy applications: Structural and mechanistic features, *Chem. Soc. Rev.* **39**, 4370 (2010).
- [6] T. Morimoto, M. Nagai, Y. Minowa, M. Ashida, Y. Yokotani, Y. Okuyama, and Y. Kani, Microscopic ion migration in solid electrolytes revealed by terahertz time-domain spectroscopy, *Nat. Commun.* **10**, 2662 (2019).
- [7] A. J. Jacobson, Materials for solid oxide fuel cells, *Chem. Mater.* **22**, 660 (2010).
- [8] N. Mahato, A. Banerjee, A. Gupta, S. Omar, and K. Balani, Progress in material selection for solid oxide fuel cell technology: A review, *Prog. Mater. Sci.* **72**, 141 (2015).
- [9] M. Mogensen, N. M. Sammes, and G. A. Tompsett, Physical, chemical and electrochemical properties of pure and doped ceria, *Solid State Ionics* **129**, 63 (2000).
- [10] S. Omar, E. D. Wachsman, J. L. Jones, and J. C. Nino, Crystal structure–ionic conductivity relationships in doped ceria systems, *J. Am. Ceram. Soc.* **92**, 2674 (2009).
- [11] R. D. Shannon, Revised effective ionic radii and systematic studies of interatomic distances in halides and chalcogenides, *Acta Crystallogr., Sect. A* **32**, 751 (1976).
- [12] J. A. Kilner and R. J. Brook, A study of oxygen ion conductivity in doped non-stoichiometric oxides, *Solid State Ionics* **6**, 237 (1982).
- [13] See the Supplemental Material at <http://link.aps.org/supplemental/10.1103/PhysRevApplied.16.064069> for SEM photographs of the samples, analysis of infrared reflection spectra, the influence of the high-temperature silica tube on THz spectroscopy, and the conductivity spectra of related zirconia sintered pellets.
- [14] K.-R. Lee, J.-H. Lee, and H.-I. Yoo, Grain size effect on the electrical properties of nanocrystalline ceria, *J. Eur. Ceram. Soc.* **34**, 2363 (2014).
- [15] S. Mochizuki, Infrared optical properties of cerium dioxide, *Phys. Status Solidi B* **114**, 189 (1982).
- [16] N. I. Santha, M. T. Sebastian, P. Mohanan, N. M. Alford, K. Sarma, R. C. Pullar, S. Kamba, A. Pashkin, P. Samukhina, and J. Petzelt, Effect of doping on the dielectric properties of cerium oxide in the microwave and far-infrared frequency range, *J. Am. Ceram. Soc.* **87**, 1233 (2004).
- [17] T. Gürel and R. Eryiğit, Ab initio pressure-dependent vibrational and dielectric properties of CeO₂, *Phys. Rev. B* **74**, 014302 (2006).
- [18] C. Klingshirn, *Semiconductor Optics* (Springer, Berlin, 2005).
- [19] J. Koettgen, T. Zacherle, S. Grieshammer, and M. Martin, Ab initio calculation of the attempt frequency of oxygen diffusion in pure and samarium doped ceria, *Phys. Chem. Chem. Phys.* **19**, 9957 (2017).
- [20] J. Koettgen and M. Martin, The effect of jump attempt frequencies on the ionic conductivity of doped ceria, *J. Phys. Chem. C* **123**, 19437 (2019).
- [21] B. Ferguson and X.-C. Zhang, Materials for terahertz science and technology, *Nat. Mater.* **1**, 26 (2002).
- [22] K. Sakai, *Terahertz Optoelectronics* (Springer, Berlin, 2005).
- [23] J. Neu and C. A. Schmuttenmaer, Tutorial: An introduction to terahertz time domain spectroscopy (THz-TDS), *J. Appl. Phys.* **124**, 231101 (2018).
- [24] B. Bulfin, A. J. Lowe, K. A. Keogh, B. E. Murphy, O. Lübben, S. A. Krasnikov, and I. V. Shvets, Analytical model of CeO₂ oxidation and reduction, *J. Phys. Chem. C* **117**, 24129 (2013).
- [25] I. K. Naik and T. Y. Tien, Small-polaron mobility in non-stoichiometric cerium dioxide, *J. Phys. Chem. Sol.* **39**, 311 (1978).
- [26] L. Pálfalvi, J. Hebling, J. Kuhl, Á Péter, and K. Polgár, Temperature dependence of the absorption and refraction of Mg-doped congruent and stoichiometric LiNbO₃ in the THz range, *J. Appl. Phys.* **97**, 123505 (2005).
- [27] Da Yu Wang, D. S. Park, J. Griffith, and A. S. Nowick, Oxygen-ion conductivity and defect interactions in yttria-doped ceria, *Solid State Ionics* **2**, 95 (1981).
- [28] S. B. Adler and J. W. Smith, Effects of long-range forces on oxygen transport in yttria-doped ceria: Simulation and theory, *J. Chem. Soc., Faraday Trans.* **89**, 3123 (1993).
- [29] K. Fuda, K. Kishio, S. Yamauchi, K. Fueki, and Y. Onoda, ¹⁷O NMR study of Y₂O₃-doped CeO₂, *J. Phys. Chem. Solids* **45**, 1253 (1984).
- [30] M. Nakayama and M. Martin, First-principles study on defect chemistry and migration of oxide ions in ceria doped

- with rare-earth cations, *Phys. Chem. Chem. Phys.* **11**, 3241 (2009).
- [31] J. E. Bauede and J. Hxizo, Interpretation of the resistivity temperature dependence of high purity $(\text{ZrO}_2)_{0.90}(\text{Y}_2\text{O}_3)_{0.10}$, *J. Phys. Chem. Solids* **30**, 565 (1969).
- [32] O. Yamamoto, Y. Arachi, H. Sakai, Y. Takeda, N. Imanishi, Y. Mizutani, M. Kawai, and Y. Nakamura, Zirconia based oxide Ion conductors for solid oxide fuel cells, *Ionics* **4**, 403 (1998).
- [33] R. Pornprasertsuk, P. Ramanarayanan, C. B. Musgrave, and F. B. Prinz, Predicting ionic conductivity of solid oxide fuel cell electrolyte from first principles, *J. Appl. Phys.* **98**, 103513 (2005).
- [34] H. Yoshida, H. Deguchi, K. Miura, M. Horiuchi, and T. Inagaki, Investigation of the relationship between the ionic conductivity and the local structures of singly and doubly doped ceria compounds using EXAFS measurement, *Solid State Ionics* **40**, 191 (2001).
- [35] J. P. Dahl, The morse oscillator in position space, momentum space, and phase space, *J. Chem. Phys.* **88**, 4535 (1988).
- [36] S. Shin and M. Ishigame, Defect-induced hyper-Raman spectra in cubic zirconia, *Phys. Rev. B* **34**, 8875 (1986).
- [37] M. Sternik and K. Parlinski, Lattice vibrations in cubic, tetragonal, and monoclinic phases of ZrO_2 , *J. Chem. Phys.* **122**, 064707 (2005).